A SURROGATE-BASED APPROACH FOR UNCERTAINTY ANALYSIS OF THE ONERA 7A ROTOR

Manas Khurana
Science and Technology Corporation
Ames Research Center, Moffett Field, CA, USA

Hyeonsoo Yeo
US Army Combat Capabilities Development Command
Aviation & Missile Center
Ames Research Center, Moffett Field, CA, USA

Abstract

An uncertainty quantification framework for rotorcraft applications is introduced. The capabilities of the developed approach are demonstrated using the ONERA 7A rotor at high-speed to model the uncertainties in blade properties including torsion, flap, and lag stiffness on rotor power and loads including torsion, flap bending, and chord bending moments. To support large-scale simulations which are needed to establish statistical convergence, a surrogate-based framework is introduced using an artificial neural network that is conceptualized, trained, and validated using data derived from rotorcraft comprehensive analysis code. The analysis characterizes the input uncertainties as aleatory, hence are normally distributed. Through propagation it is established that the uncertainties in rotor power are limited; moderate for peak torsion moment; and significant for peak flap bending and chord bending moments. The analysis further quantified that uncertainties in spanwise flap bending moment are present and are influenced by the variability in flap and torsion stiffness. The results demonstrate the integration of a probabilistic-based framework to a surrogate-based approach for the quantification of system uncertainties to facilitate informed decision making based on model-based predictions.

Notation

r/R - Blade Radial Station
CA - Comprehensive Analysis
CBM - Chord Bending Moment
CDF - Cumulative Distribution Function
FBM - Flap Bending Moment
GEV - Generalized Extreme Value distribution
LHS - Latin Hypercube Sampling
MCS - Monte Carlo Simulations
MLE - Maximum Likelihood Estimation
QoI - Quantity of Interest
PDF - Probability Density Function
R - Correlation Coefficient
SF - Scaling Factor (blade stiffness)
TM - Torsion Moment
UQ - Uncertainty Quantification

1. Introduction

Modeling and simulation is integral in rotorcraft research and development where multidisciplinary simulation codes such as CREATE^{TM}-AV Helios [1] and Rotorcraft Comprehensive Analysis System (RCAS) [2] have been developed, validated, and used for the analysis of existing and novel rotorcraft configurations. Traditional computational analysis follows a deterministic-based approach where model inputs are propagated to the function evaluator to establish an estimate of system response. Typically there are inherent uncertainties in the inputs which limit the accuracy of the output quantify-of-interest (QoI) and confidence whether the derived data is a true representation of expected system behaviour. Ideally, a computational approach that factors the uncertainties of the system inputs to then quantify a range of response outputs with probability is a critical requirement that needs to be addressed. Accordingly, the reliance of computational tools for aerospace design has resulted in the emergence of uncertainty quantification (UQ) and sensitivity analysis (SA) disciplines. The focus of this work is to introduce a computational framework that supports the migration from traditional deterministic-based simulations that are typically exercised in rotorcraft design and analysis to a stochastic

based paradigm.

Historically the assessment of system uncertainties has been based on subjective experience-based evaluations of the simulation results. Although the approach has merits, a mathematical framework using a structured UQ approach is needed to establish the estimate of model uncertainties using the statistics of the code output due to uncertainty in the inputs. Post-processing of UQ results permit the assessment of event occurrences that represent the likelihood of reaching a critical performance threshold with probability. The identification and management of system uncertainties is critical in rotorcraft aeromechanics. To facilitate this adoption, an understanding of the sources and characterization of the uncertain inputs is needed so that model predictions that follow will enable analysts to execute informed data-driven decisions with confidence.

The analysis in this work addresses the uncertainties in component manufacturing in blade properties on rotor performance and loads. Consider fiber reinforced composite structures which at the micro-scale level are characterized with uncertainties in the matrix that binds the fiber and influences the transfer of loads between the attached fibers. At the meso-scale, uncertainties are present in the laminate stacking sequence attributed to the thickness of the attached layers and the corresponding orientation angles [3] which can be altered beyond the set design tolerances during a manufacturing process. A critical enabler that facilitates valued early decision-making is the impact of the uncertainties of different scales to ensure outputs do not exceed safety margins. This will then translate to improved decision making to mitigate risk and high costs. Accordingly, the work focuses on the development and implementation of a stochastic-based simulation tool set that will be used to model the uncertainties in blade properties on flight performance and loads. Data post-processing will then facilitate refinements to the manufacturing processes as an aid to ensure uncertainties in blade properties do not adversely limit vehicle performance and loads.

The stochastic-based framework models the uncertainties in blade torsion (GJ), flap (EI_{flap}), and lag (EI_{lag}) stiffness on rotor power and loads including torsion (TM), flap bending (FBM), and chord bending (CBM) moments for the ONERA 7A rotor at high speed. In the earlier analysis by Khurana et. al [4], effect of uncertainties in beam properties on rotor power and half peak-to-peak TM using Monte Carlo sampling with data assimilation using RCAS was presented. Although a valid approach, the practise is computationally intensive as hundreds-of-simulations were needed for a statistically converged result to then enable the interpretation of uncertainty results. This practise cannot be efficiently scaled and is not amendable to large-scale simulations if the scope of the input uncertain parameter space were to be extended. This work addresses the challenge with the integration of artificial neural networks (ANN). Similarly the uncertainties in half peak-to-peak loads are established and the data is compared to the results formed using RCAS-based simulations. The ANN methodology will also be executed to model the uncertainties in blade spanwise flap bending moment.

The paper is structured as follows: In **Section 2:** reference test model with the ONERA 7A rotor which will be used to demonstrate the UQ methodology is introduced and the RCAS solver setup is validated using experiment data; In **Section 3:** an overview of the UQ approach applied and the computational framework developed to support this effort is presented; In **Section 4:** numerical results relating to the design, development, and validation of a surrogate-based approach with ANN is presented and the integration of the surrogate-assisted approach for uncertainty propagation is presented; and in **Section 5:** work conclusions are summarized and ongoing research efforts are summarized.

2. Model

The ONERA 7A rotor is a four-bladed fully articulated rotor with a radius of 2.1m and solidity, σ, of 0.084. In the analysis, it is studied at high-speed condition (μ = 0.4, C_L/σ = 0.063), and has been investigated in the literature using various analysis tools and methods [5–8]. The rotor was trimmed to satisfy the Modane flapping law (β_{1s} = 0, $\beta_{1c} = -\theta_{1s}$) in addition to the specified rotor lift and propulsive force using rotor collective and cyclic controls and shaft angle. The blade in Figure 1, is a rectangular planform and uses the OA213 and OA209 airfoils.

The rotor was analyzed in RCAS using 16 nonlinear beam elements and 22 aerodynamic segments. The rotor hub was further modeled as fully articulated with pitch bearing and flap and lag hinges. The elastomeric lag damper of the 7A rotor was modeled with equivalent hinge stiffness and damping values at the lag hinge. The lift, drag, and pitching moment on each aerodynamic segments are calculated using airfoil characteristics from C81 lookup tables provided by ONERA. Linear unsteady airloads include classical quasi-steady Theodorsen theory. The finite state dynamic inflow model is used to calculate rotor wake flowfield.

The 7A rotor has also been tested in the ONERA S1MA transonic wind tunnel [9] and the experimental data is used to validate the RCAS model setup. As the comprehensive analysis code will be used extensively to perform larges-scale simulations with different input parameter (blade stiffness) configurations for ANN development, it was important that the CA toolset sustains acceptable balance between computational

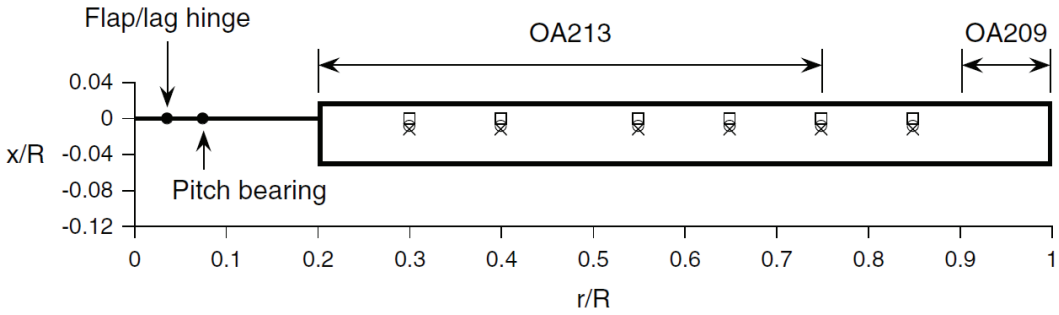

Figure 1: 7A blade planform with structural loads measurement locations (□: flap bending; ○: chord bending; and ×: torsion moment)

efficiency and agreement with wind-tunnel data. Accordingly, a finite-state dynamic inflow model based on the actuator disk solution of the three-dimensional potential flow equations is used. The induced velocity is expressed in terms of Fourier harmonics (for azimuthal variations) and Legendre functions (for radial variations). In an m-by-n dynamic inflow model, m represents the number of harmonics and n denotes to the highest power in the Legendre polynomials. Figure 2 compares RCAS predictions with measured data along the blade span.

The dynamic inflow model convergence study confirms that as the number of inflow states is increased, the RCAS predicted peak-to-peak structural loads decrease and converge to the experimental data. There was limited test data available for the spanwise CBM (Fig. 2c), yet acceptable agreement is noted at the available evaluation points and also for spanwise TM and FBM cases as the inflow states is increased. The convergence of rotor power with experimental data is also presented in Table 1 where a divergence in RCAS results with experiment is noted as the inflow state is increased. In general, the computational disparity between an 8×8 and 12×12 state model with RCAS for rotor power and structural loads is negligible, yet the computational effort is higher for the larger inflow state model. Hence, an 8×8 model will be used as the baseline setup for the follow up UQ works.

3. Uncertainty Quantification Approach

This section describes the UQ principles that are implemented to support the analysis and the uncertainty propagation scheme that will be exercised using a surrogate-based approach. An overview of the statistical metrics needed to quantify system uncertainties using a Monte Carlo approach are defined, and a brief summary of the surrogate-based approach using an ANN and the training convergence criterion applied are introduced.

The model U is considered as a black box and represents the underlying system, in this case RCAS, which is analyzed by solving the governing equations. Here f is the general model with output, Y, such that $Y = f(\boldsymbol{x})$, where $\boldsymbol{x} = [x_1, x_2, \ldots, x_k]^T$ is a vector of k inputs to the model with associated probability distributions.

$$Y = f(\boldsymbol{x}) \tag{1}$$

The output Y is any value in the output space ΩY with an unknown probability density function ρ_Y that is established using a uncertainty propagation scheme. This involves the determination of the distribution of Y for function f in Equation 1 based on the distributions of the input parameters of $\boldsymbol{x}$ in probability space ΩY. The uncertain input parameters to facilitate uncertainty propagation are sampled from a Normal (Gaussian) distribution with mean, μ, and standard deviation, σ. The probability density function (PDF) of the Normal distribution, $\rho_N(\boldsymbol{x})$ is denoted $N(\mu, \sigma)$ by:

$$\rho_N(\boldsymbol{x}) = \frac{1}{\sigma\sqrt{2\pi}} e^{-\frac{1}{2}\left(\frac{x-\mu}{\sigma}\right)^2} \tag{2}$$

The UQ metrics are established from the statistics of the output distribution ρ_Y using the mean, $\mathbb{E}$ (expectation value) and variance, $\mathbb{V}$. The mean is defined as:

$$\mathbb{E}[Y] = \int_{\Omega Y} \boldsymbol{x}\rho_Y(\boldsymbol{x})d\boldsymbol{x}, \tag{3}$$

where ρY is the joint probability density function of the random inputs, $\boldsymbol{x}$. The related statistical measures are calculated from ρY using statistical moment, i, with Equation 4 representing the variance ($i = 2$):

$$\mathbb{V}[Y] = \int_{\Omega Y} (\boldsymbol{x} - \mathbb{E}[Y])^{i=2}\rho_Y(\boldsymbol{x})d\boldsymbol{x}, \tag{4}$$

where the i^{th} moment represents the variance ($i = 2$), skewness ($i = 3$), and kurtosis ($i = 4$).

UQ data post-processing further involves the representation of the output distribution, ρ_Y, into a cumulative distribution function (CDF) that is representative of the area under the PDF. It is used to evaluate the probability, P, that output Y will take a value less than

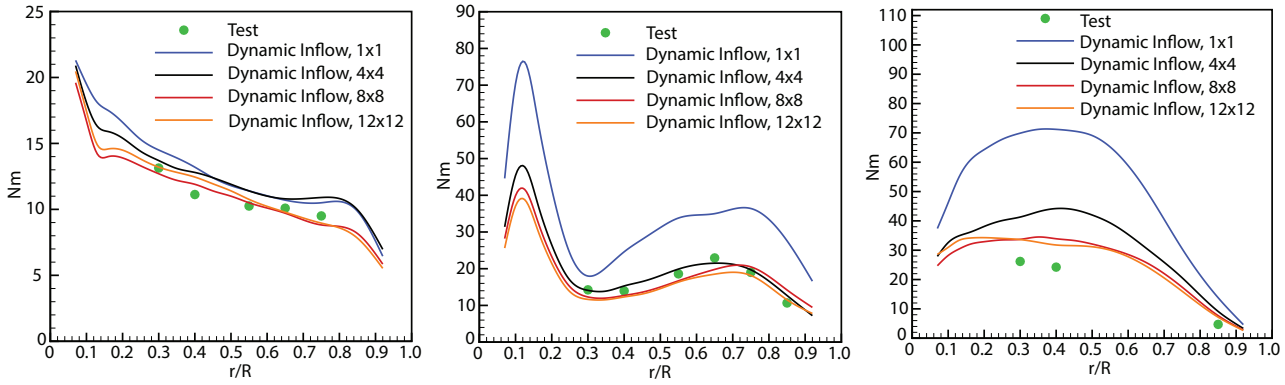

(a) Torsion moment [Nm] (b) Flap bending moment [Nm] (c) Chord bending moment [Nm]

Figure 2: Half peak-to-peak structural loads: convergence of dynamic inflow model with test data using RCAS

Table 1: Validation of rotor power as a function of dynamic inflow model with test data

	Power [HP]
Test	118.16
Dynamic inflow, 1×1	113.33
Dynamic inflow, 4×4	124.46
Dynamic inflow, 8×8	124.81
Dynamic inflow, 12×12	125.02

or equal to set threshold, y such that:

$$f_Y(y) = P(Y \leq y) \tag{5}$$

The probability that Y is in the interval $(a, b]$ such that $a < b$ is denoted by:

$$P(a < Y \leq b) = f_y(b) - f_y(a) \tag{6}$$

The CDF permits the assessment of critical design questions, for example: *What is the probability that rotor power is less than x given the uncertainty in blade torsion stiffness?* Equation 6 will be primarily used as a quantifying measure to represent the uncertainties of the system in the results to follow.

3.1. Uncertainty Propagation analysis Method

A. Monte Carlo approach

The widely used probabilistic approach for uncertainty propagation is the Monte Carlo method. The framework can facilitates UQ in a non-intrusive manner as it does not require the modification of the underlying solver, and it also does not make any assumptions about the model. The method randomly selects the input parameters from the input PDF's across the ranges of uncertain variables, $\boldsymbol{x}$, of size nS by a stratified sampling scheme. The model is then evaluated at sample $\boldsymbol{x}$ that creates the mapping of the inputs to outputs:

$$[\boldsymbol{x_i}, y_i], i = 1, 2, \ldots, nS \tag{7}$$

where $y_i = f(\boldsymbol{x_i})$. Equations 3 and 4 are used to calculate the statistics of the response output, y, and the process is repeated until statistical convergence of y is achieved. The mapping in Equation 7 can be post-processed using scatterplots to assess the relationships (linear, non-linear, discontinuities) between inputs and outputs, or a least squares approach can also be applied to form a regression model that relates output to inputs. Statistical relationships can then be inferred between $\boldsymbol{x}$ and y in a computationally efficient manner rather than directly simulating the underlying model using ANN.

Uncertainty propagation with MC simulations will converge to the exact stochastic solution as the sample population, $N \to \infty$. As per the law of large numbers, model mean and variance are established by:

$$\mathbb{E}[Y] \approx \overline{y}_N = \frac{1}{N} \sum_{m=1}^{N} f(\boldsymbol{x}^m), \tag{8}$$

$$\mathbb{V}[Y] \approx \frac{1}{N-1} \sum_{m=1}^{N} (f(\boldsymbol{x}^m) - \overline{y}_N)^2, \tag{9}$$

where N is the total number of model evaluations in the simulation; $\overline{y}_N$ is sample mean of output y from N

runs; and $\boldsymbol{x}^m = [x_1^m, x_2^m, \ldots, x_k^m]^T$ represents the m^{th} sample realization of the random input vector $\boldsymbol{X}$. Yet, convergence of the mean error estimate will be limited as the standard deviation of the mean scales inversely with the square root of the sample size:

$$\sigma_\mu = \frac{\sigma}{\sqrt{N}} \tag{10}$$

Hence, a significant limitation of the MC approach is that it requires a large number of function evaluations for statistical convergence. One approach to limit this issue involves improving the coverage of the parameter space for the distribution of the input samples. Accordingly Latin hypercube sampling (LHS) developed by McKay [10] is used for uncertainty propagation. In this approach, the range of each input random variable is divided into intervals with equal probability. The methodology has been extensively used in a wide range of applications [11–15], including rotorcraft conceptual design [16] and uncertainty analysis with NASA rotorcraft sizing design tools [17]. Even with improved stratified sampling for uncertainty propagation, the MC approach with direct model evaluations is a computationally expensive process especially if high-fidelity simulations govern the solver. To adequately address this issue, a metamodel is needed for the system response.

B. Artificial Neural Networks

Surrogate modeling is implemented to replace a computationally expensive deterministic model for accurate and efficient approximation of the data from RCAS. Mathematically the methodology is defined as follows (notation adopted from Gorissen et al. [18]): Surrogate modeling is used in the design process to approximate a multivariate function $f : \Omega \mapsto \mathbb{C}^n$, in a user-defined domain $\Omega \subset \mathbb{R}^d$, where the corresponding function values $f(x) = [f(x_1, \ldots, f(x_k)] \in \mathbb{C}^n$ are the computed measure of power and loads of sampled blade input stiffness properties $X = \{x_1, \ldots, x_k\} \subset \Omega$ from RCAS. The development of a metamodel requires the definition of a function s, from approximation space, $\mathcal{S}$, such that $s : \mathbb{R}^d \mapsto \mathbb{C}^n \in \mathcal{S}$, where s is closely related to f, and the measure of similarity is assessed by the approximation error $||f - s||_v$, according to a user-defined norm $||.||_v$. The metamodel must be developed to yield an acceptable approximation of $s^* \in \mathcal{S}$, such that s^* it is in accordance to $\min_{s\in\mathcal{S}}||f - s||_v = ||f - s^*||_v$. It is assumed that the input data and the corresponding outputs from RCAS are deterministic and noise free, hence facilitating an accurate metamodel where the approximation error between f and s is minimised.

The ANN framework [19] is used as the surrogate tool in this work and the methodology has been widely applied in the literature for aerospace design analysis [20–26] and to support uncertainty quantification studies [27–31]. The MATLAB Neural Network Toolbox [32] is integrated into the computational framework to support the research efforts. A series of ANN topologies are conceptualized that map the relationship between the variation in blade stiffness properties as inputs on rotor power and: **(a)** half peak-to-peak moment; and **(b)** spanwise flap bending moment as outputs.

As fist step in ANN development, the inputs and outputs are normalized between [0,1]. The networks considered are feed-forward with single or double hidden-layers where in each layer there are 10-40 neurons. The $tan - sigmoid$ transfer function is used in the hidden layers and a linear function for output representation. Network training is performed using the Levenberg–Marquardt algorithm [32]. The sample set used for model development and validation is partitioned such that 70% of the total dataset is used for training; 15% for validation and 15% for testing. The validation set are independent data points that are used to assess the generalization capabilities of the network at each training epoch such that the mean-squared-error, (mse), is calculated by the difference between target and ANN approximated outputs. If the mse increases over successive user-defined iterations, then ANN training is terminated to ensure the network is not overfitted. The testing points are an additional set of independent points that are further used to assess the accuracy of the ANN at each iteration and do not directly influence the training and training termination criteria. Network performance on the identified data points (training, testing, validation) is further assessed by the calculation of the correlation coefficient, r that is assessed between target values and ANN outputs.

3.2. Analysis Setup

A. Computational Setup

A computational framework is developed to support the simulations in an automated manner. The uncertainty analysis is formulated and executed using DAKOTA [33]. To orchestrate the simulations using parallel computing, the Galaxy Simulation Builder [34] developed by the Department of Defense (DoD) is used that permits users to create large-scale simulations in a logical piece-by-piece manner with the added capability to schedule and monitor the jobs using a web-interface. The workflow developed is presented in Figure 3.

The automated workflow is comprised of five modules. In **Module one:** The DAKOTA input file is formed where the study mode is defined, in this case, uncertainty analysis, and the uncertain input parameters are labelled and the PDFs of the aleatory parameters are defined; **Module two:** an RCAS input file is added and identifiers are inserted into the template file for variable substitution; **Module**

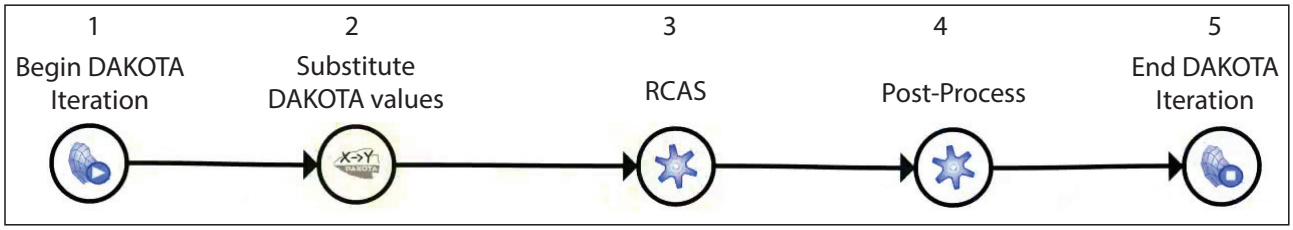

Figure 3: Graphical representation of the computational setup using GALAXY with DAKOTA

three: the RCAS executable is added to the workflow path; **Module four:** MATLAB post-processing scripts are introduced that utilize the outputs from RCAS simulations, in this case, the structural loads, to then calculate the statistical metrics needed to quantify the uncertainty limits using the probability intervals; and **Module five:** DAKOTA simulation is terminated once a user-defined termination criterion from module one is satisfied.

B. Parametric Analysis

The computational framework is now demonstrated to perform parametric analysis by inducing systematic variations of blade stiffness on rotor power and structural bending moment. The goal of this exercise is to confirm that the automated design processes developed will operate seamlessly which is a critical requirement for the large-scale uncertainty simulations to follow. This exercise will further quantify if linear and/or non-linear relationships follow between stiffness properties on rotor performance and loads. This is important as it will confirm that multi-dimensional input spaces are often multi-modal and a simplified parametric based approach about a select baseline point is not sufficient to quantity system probabilities needed for uncertainty analysis. Instead, large-scale data sampling using stratified approaches such as the LHS method becomes a requirement.

A key parameter that will be used in the analysis is the blade stiffness scaling factor (SF). The SF acts as a multiplier to the baseline stiffness, denoted by SF=1.0, to induce systematic and *uniform* variations from blade root to tip for torsion (GJ), flap (EI_{flap}) and lag (EI_{lag}) stiffness. Figure 4 shows the envelope of the variations in domain, $0.40 \leq$ SF ≤ 2.0, that will be used for the parametric and uncertainty analysis.

In Figure 4, blade inboard sections are characterized with high stiffness variations relative to outboard sections where stiffness distributions remains consistently low. As next step, the relationships between stiffness on power and bending moment is established by varying the SF *uniformally* one-at-a-time with other properties fixed at the baseline setting (SF=1.0). At each incremental change, rotor power and structural loads are calculated using RCAS. Figure 5 shows the resulting effect of the one-factor variations in GJ, EI_{flap} and EI_{lag} on power.

The analysis confirmed that power is sensitive to changes in GJ, and relatively power remains unchanged due to the variability in lag and flap stiffness. Critically it is noted that there is a penalty in rotor power as GJ decreases. In the earlier analysis by Jain and Yeo [35], this pattern was also established with the UH-60A rotor in high-speed forward flight. This was attributed to the distribution of the average drag across the rotor disk which was observed to increase as GJ was decreased such that there was a higher drag penalty on the outboard region of the retreating side. Accordingly, an increase in rotor power follows to maintain trimmed flight.

Figure 6 represents the variation in stiffness using the SF for torsion, flap, and chord bending moments. Here it is observed that as GJ increases (Fig. 6a), the torsion moment decreases slightly. In general, the torsion stiffness changes have small influence on torsion moments except for the significant reduction of GJ at SF=0.40. The baseline torsion frequency is about 6/rev. As torsional stiffness is reduced, torsion frequency also decreases. Initially there is small change in the peak-to-peak amplitude. However, as the torsion frequency approaches 4/rev, the peak-to-peak loads starts to increase.

The impact of flap stiffness on spanwise flap bending moment is further presented in Figure 6b. Flap stiffness has a significant influence on flap bending moment. As expected, the spanwise flap bending moment increases, including the maximum peak-to-peak load at r/R $\approx$ 0.125 as EI_{flap} increases. The variation in lag stiffness on chord bending moment is also modeled in Figure 6c. Chord bending moment results show complicated, non-linear response with respect to the lag stiffness variation. The baseline lag frequency is 4.44/rev, which avoids harmonics of rotation frequency that can lead to resonances. As blade stiffness is increased or decreased, lag frequency approaches 5/rev and 4/rev and the blade chord bending moment amplitude increases. As the blade frequency further increases away from the resonance, the blade chord bending moment decreases. However, the baseline stiffness value still provides minimum half peak-to-peak chord bending moment.

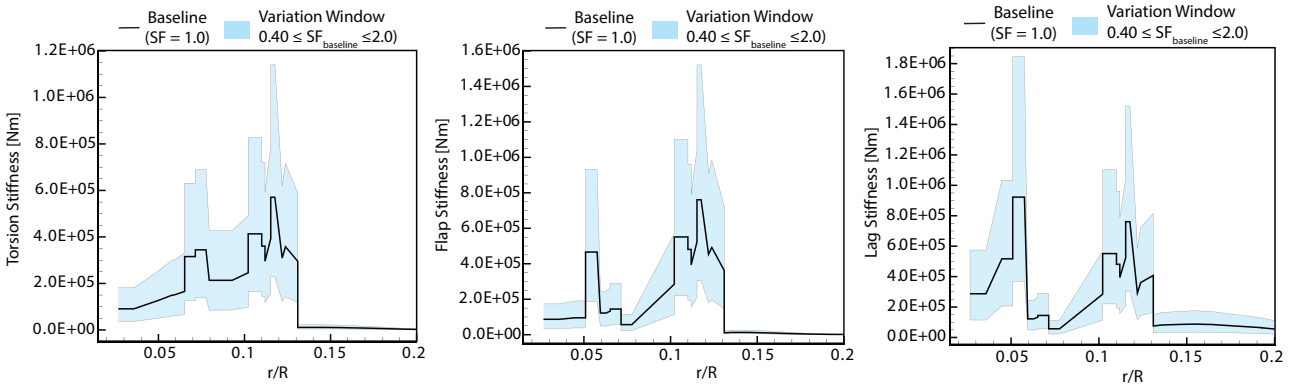

(a) GJ (b) EI_{flap} (c) EI_{lag}

Figure 4: Blade stiffness parametric analysis test envelope using a scaling factor (SF)

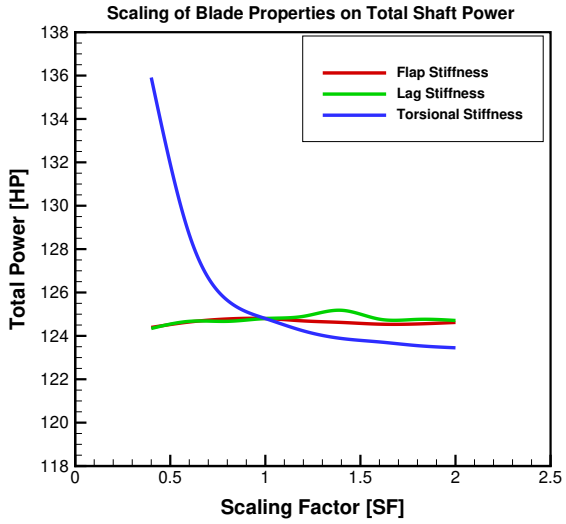

Figure 5: Impact of blade stiffness variation on rotor power [HP]

C. Uncertainty Analysis Setup

In the uncertainty work to follow, the SF of each blade property will be used as the uncertain variable and will be perturbed using a prescribed probability distribution. Recall, the scaling factor will induce *uniform* variability in stiffness from blade root-to-tip. The SF is characterized as an aleatory uncertain parameter due to the inherent randomness in spanwise blade properties as a result of manufacturing variations. The classification of input uncertainties are defined in Table 2. Here, the SF is assumed to be normally distributed with mean, $\mu = 1.0$ (blade at baseline state) with a standard deviation of $\sigma = 20\%$ (variability of uncertainty about the nominal state). In absence of raw material data that can be used to confirm the expected variability in blade properties of manufactured blades from a large-scale production line, in this analysis, the expected variability is assumed to follow a normal distribution curve and may not represent real-life distributions. Yet, the goal here is to demonstrate the workings of the applied UQ methodology that would translate the input distributions to output uncertainties.

4. Numerical results

In this section, the setup and execution of a surrogate-based approach for uncertainty analysis is presented. The cases will model the collective uncertainties in blade stiffness parameters on: **(a)** half peak-to-peak bending moment; and **(b)** spanwise flap bending moment. ANN model setup, training, and validation will be presented as a starting point for each case followed by the simulation of the developed framework to facilitate uncertainty propagation.

4.1. ANN Development: GJ, EI_{flap}, EI_{lag} $\rightarrow$ power & half peak-to-peak load

The ANN is trained and validated using the existing dataset of solutions that were generated in previ-

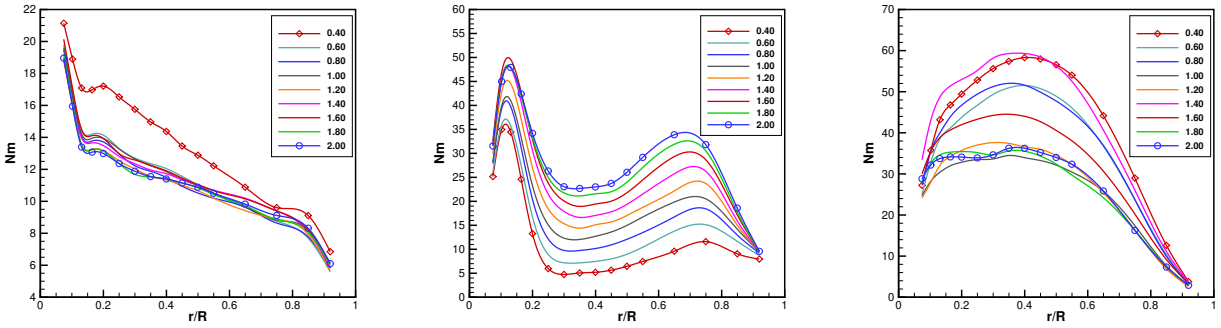

(a) GJ on torsion moment (b) EI$_{flap}$ on flap bending moment (c) EI$_{lag}$ on chord bending moment

Figure 6: Spanwise distribution of bending moment due to variability in stiffness spanning 40% to 200% relative to baseline

Table 2: Representation of uncertain stiffness input parameters to establish impact on rotor power and structural loads (torsion, flap, & chord bending moments)

Stiffness	Parameter (SF)	PDF	mean (μ)	std. dev.
GJ	SF$_{\text{GJ}}$	Normal	1.0	0.20
EI$_{\text{flap}}$	SF$_{\text{EI}_{YY}}$	Normal	1.0	0.20
EI$_{\text{lag}}$	SF$_{\text{EI}_{ZZ}}$	Normal	1.0	0.20

ous exercises for uncertainty propagation using stand-alone RCAS with Monte Carlo simulations (MCS). The repository included 700 input stiffness parameters that were collectively permutated and mapped to response outputs calculated over 6 hours serially on a standard Linux-based desktop system. Table 3 represents the performance of the ANN trained using 490 points with the accuracy assessed on 210 testing points that have no influence on network training.

The results in Table 3 confirm that the ANN yields acceptable accuracy in predicting rotor power and half peak-to-peak loads. An $r-$coefficient $>$ 0.90 represents strong positive correlations between ANN predictions and target RCAS values, yet the accuracy in predicting TM$_{max}$ (shaded cell in Table 3) is limited with a lower $r-$coefficient than the other cases modeled.

To understand this result, a scatter plot of the 210 test points representing ANN predictions versus RCAS target values is presented using histograms in Figure 7. The $x-$axis of the histograms represents the distribution of the blade stiffness parameter design space that was sampled to train the ANN. Recalling the input parameters were assumed to be uncertain using a normal distribution curve. The diagonal line in the regression chart (middle subset in Fig. 7) represents the line-of-best fit denoting a perfect agreement between ANN approximation versus RCAS. It is observed that most of the 210 test points quantified by the ANN are characterized with acceptable agreement relative to target as the points are projected on the line-of-best fit. It is also established that there are two extreme outliers, under the dotted circle in the regression chart, that are characterized with limited ANN approximation capabilities that result in the lowering of the $r-$coefficient (shaded cell in Table 3). As next steps, the input stiffness parameters corresponding to each of the modeled TM$_{max.}$ outputs in the test dataset regression coefficient chart is projected using an histogram. It is noted that outlier 1 is characterized with a flap stiffness of EI$_{flap}$=0.49; and outlier 2 is denoted with GJ=0.42. The histogram shows that both outliers are at the tail ends of the normal distribution curve that is used to define the aleatory representation of the uncertainty in blade stiffness. At these extreme regions, the training dataset used for ANN development is limited and the corresponding accuracy of the surrogate model is adversely affected, hence resulting in the lowering of the $r-$coefficient. Further, the stiffness magnitudes at the tail regions is extreme relative to the baseline setting with stiffness one, and such extreme variations in blade properties would not be expected due to variability in manufacturing tolerances. Using the ANN for uncertainty propagation or design parametric analysis, it is reasonable to constrain the blade stiffness to values about the baseline so that these extreme regions are not considered in the computational analysis. To demonstrate the relationship between the goodness-of-fit of the ANN using the $r-$coefficient in Table 3 against target RCAS response, a parametric analysis with variation in blade stiffness on rotor power and half peak-to-peak bend-

Table 3: ANN generalization capabilities assessed on the 210 testing points

Uncertain Inputs	Train Size	Test Size	Power	TM	FBM	CBM
				$r-$coefficient		
GJ, EI_{flap}, EI_{lag}	490	210	0.999	0.966	0.996	0.992

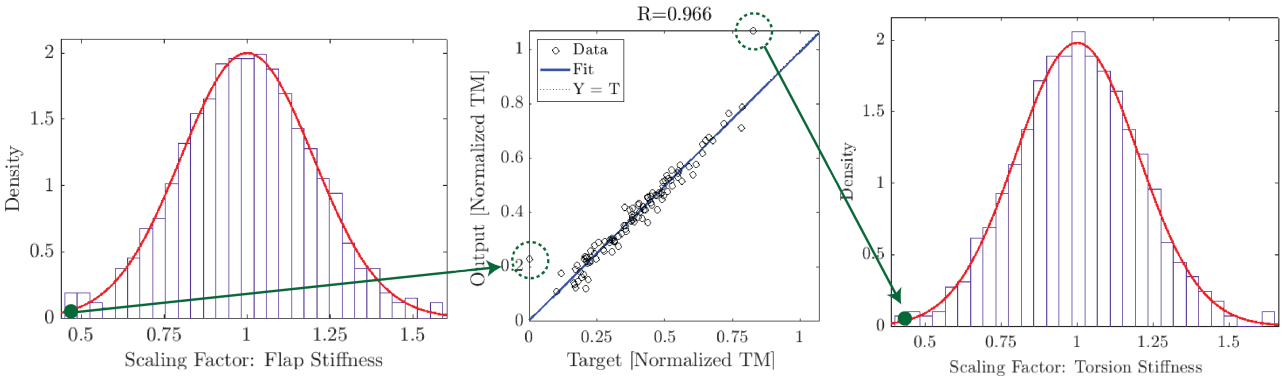

Figure 7: Representation of ANN generalization capabilities for TM_{max} using the $r-$coefficient regression with accompanying data histogram

ing moment is presented in Figures 8 and 9 respectively. In this analysis, the scaling factor for blade stiffness variability is modeled between a test envelope of $0.40 \leq$ SF ≤ 1.60. Variation in GJ on power in Figure 8a validates acceptable agreement between surrogate predictions and RCAS. Yet, at design space end point with SF≈0.40, the ANN prediction does not match RCAS. Recall the ANN is trained with data sampled from a normal distribution curve representing the assumed uncertainty in blade stiffness such that, $\mathcal{N}(\mu, \sigma)$=$\mathcal{N}(1.0, 0.20)$ (Table 2). By true definition, data sampled from a normal distribution curve will have limited points, in this case ANN training data at the tail ends of the curve, and the resulting generalization capability of the surrogate model, in this case at SF=0.40 is compromised. Yet, blades with extreme stiffness properties such that SF>1.40, the ANN continues to demonstrate acceptable convergence with RCAS target.

Similarly the parametric analysis with variability in flap stiffness in Figure 8b, confirms that ANN predictions are compromised at design space boundaries, both with soft and stiff blade settings such that SF=0.40 and SF=1.60 respectively. Relatively the agreement between the two datasets at other SF conditions is acceptable. Despite the noted qualitative differences, quantitatively the absolute magnitude between the two datasets is negligible, hence confirming the accuracy of the ANN in predicting rotor power with variability in EI_{flap} even at design space boundary. Similar patterns are also noted in Figure 8c with the assessment of rotor power due to variability in EI_{lag}. The ANN yields acceptable accuracy in converging to RCAS target with subtle qualitative divergence observed between $1.40 \leq$ SF ≤ 1.60 regions where the ANN under predicts rotor power, but quantitatively these differences are negligible.

Parametric analysis is also undertaken to assess the prediction capability of the ANN to resolve peak-to-peak loads with variation in blade stiffness spanning $0.40 \leq$ SF ≤ 1.60 in Figure 9. Perturbation of SF for GJ in Figure 9a and EI_{flap} in Figure 9b confirms that the ANN has validated accuracy in resolving peak TM and FBM respectively over the modeled test range. In Figure 9c, representing the variation in EI_{lag} on peak CBM, the ANN converges to RCAS target, yet qualitative differences are noted between $1.40 \leq$ SF ≤ 1.60 regions (tail ends of the normal distribution curve) with the ANN under predicting the peak CBM. At SF=1.40, $CBM_{max.}$ is under predicted with ANN by $\approx 4.0\%$ relative to RCAS, and at SF=1.60 the difference is extreme at $\approx 16.0\%$. Despite this high divergence between the datasets, the noted errors are at design space boundary where stiff rotor blades are present, and in reality it would not be expected that blade stiffness will deviate by this significant magnitude relative to baseline at SF=1.0 due to manufacturing tolerances. The high ANN approximation errors at the tail ends of the design space envelope can be neglected by constraining the design space to regions about the mean stiffness at SF=1.0 to ensure the results of the uncertainty analysis are not compromised by false peak-to-peak loads.

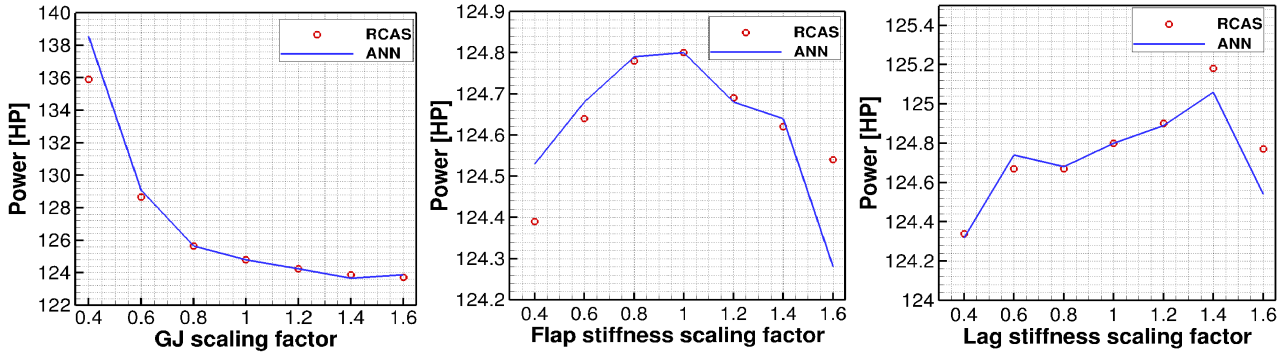

(a) GJ (b) EI_{flap} (c) EI_{lag}

Figure 8: Evaluation of rotor power prediction using ANN with RCAS

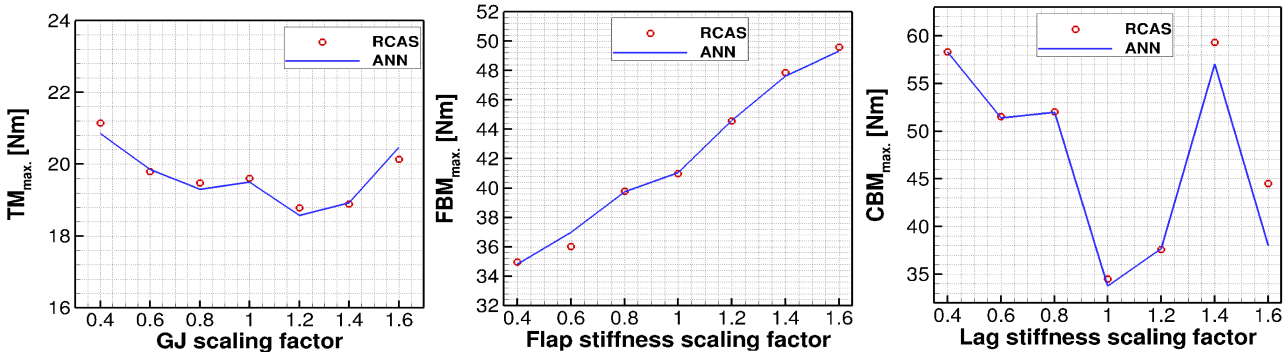

(a) GJ on $\text{TM}_{max.}$ (b) EI_{flap} on $\text{FBM}_{max.}$ (c) EI_{lag} on $\text{CBM}_{max.}$

Figure 9: Evaluation of half peak-to-peak bending moment prediction using ANN with RCAS

4.2. Uncertainty Analysis: GJ, EI_{flap}, EI_{lag} $\rightarrow$ power & half peak-to-peak load

As the accuracy of the ANN has been validated, the surrogate-based approach is now implemented to quantify the uncertainties in rotor power and half-peak-to-peak bending moment due to variability in blade stiffness that is induced using a scaling factor with prescribed aleatory distributions (Table 2). The results projected in Figure 10 represent the expected uncertainties of the output QoI established through a Monte Carlo simulation with 500,000 data points denoted by the solid blue line (—). The uncertain limits are formed using the 95% probability interval and represent outputs for SF (GJ, EI_{flap}, EI_{lag}) that is sampled using LHS from the input normal distribution curve. The sampling design space is further restricted to domain, $0.60 \leq \text{SF}_{GJ,Flap,Lag} \leq 1.40$ to avoid ANN generalization at the tail ends of the normal distribution curve that is associated with higher approximation errors (Fig. 7), and to limit the analysis to realistic (not extreme) stiffness settings that are likely due to manufacturing defects. In the results, the red bullet (•) further represents the QoI at the nominal stiffness setting, SF=1.0.

In Figure 10a, it is shown that rotor power will vary between ≈ 124.00 and 127 HP due to blade stiffness uncertainties. The baseline result representing the rotor blade at nominal stiffness is 124.80 HP and is closer to the lower limit of the established 95% probability interval range at $\approx$ 124.00 HP. Although not shown here, it was established that the PDF of output power was non-symmetrical and positively skewed, hence justifying the close proximity of the baseline result to the lower interval limit. Further, the uncertain interval range is $\approx 2.50\%$ of baseline, hence confirming that the uncertain envelope in rotor power is not significant.

Similarly, the uncertainty in $\text{TM}_{max.}$ is modeled in Figure 10b. In this result, the half peak-to-peak TM varies between $\approx 18.00 - 22.00$ Nm due to the collective uncertainties in blade stiffness properties. In this case, the baseline result is closer to the upper limit of the 95% probability interval as the output PDF is negatively skewed. The overall width of the uncertain range is significant at $\approx 10\%$ of the baseline result when no uncertainties are considered. Due to the significant uncertain envelope range, additional statistical interpretation using a CDF is warranted to quantify the expected probability that $\text{TM}_{max.}$ may exceed a critical threshold due to property uncertainties. If it

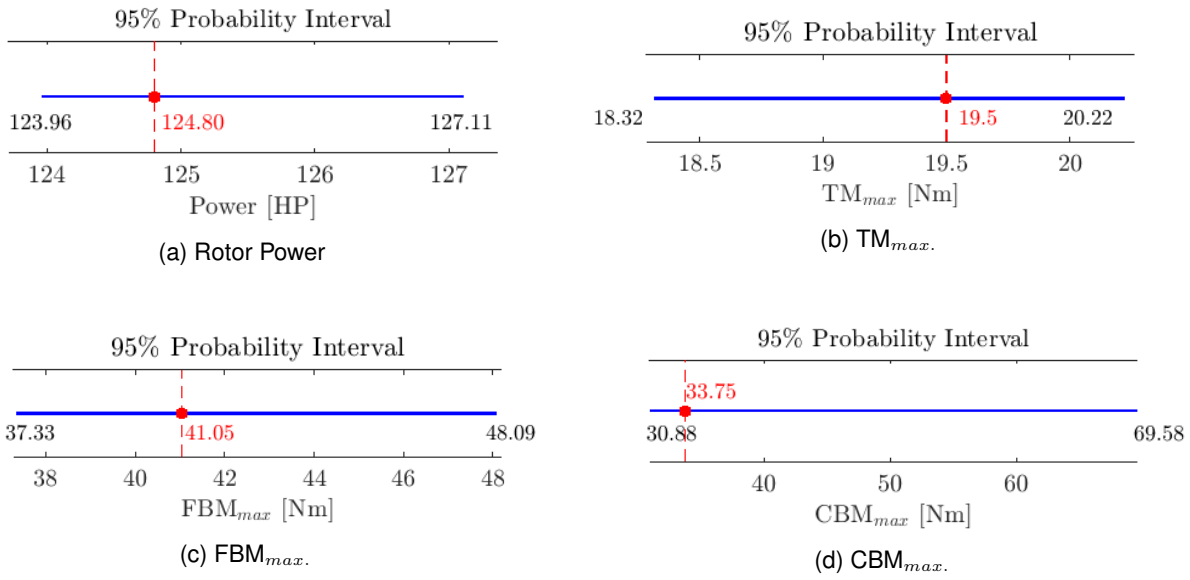

(a) Rotor Power

(b) TM$_{max.}$

(c) FBM$_{max.}$

(d) CBM$_{max.}$

Figure 10: Symmetric 95% probability interval widths of the ONERA 7A blade resulting from aleatory uncertainty propagation (bullet symbol [•] = baseline result at SF=1.0; [—-] = stochastic result with 95% probability intervals) using 500,000 LHS formed points

is assumed that the maximum upper limit of TM$_{max.}$ cannot exceed baseline at 19.50 Nm, then the probability that TM$_{max.} \leq 19.50$ is $\approx 80\%$. The merits of incorporating a stochastic-based framework to equate expected loads with probabilities due to input uncertainties is realized through this effort.

As next step, the uncertainty in FBM$_{max.}$ is presented in Figure 10c. The expected moment range due to property uncertainty is $\approx 37 - 48$ Nm which is significant at $\approx 26\%$ of the baseline result at 41.05 Nm. The PDF of FBM$_{max.}$ is also positively skewed (not shown here), hence justifying the skew of the baseline result toward the lower end of the 95% probability interval. As the expected uncertainty range in FBM$_{max.}$ is extreme, data post-processing is undertaken using the CDF formed from the Monte Carlo samples to establish the relative probabilities. If it is assumed that FBM$_{max.}$ baseline at 41.05 Nm is a critical load threshold that must not be exceeded, then the probability that this condition will be violated is $1 - Pr \leq 41.05$ = 1-0.40 = $\approx 60\%$. The high probability of system failure as a result of exceeding a maximum allowable FBM threshold will need to be analyzed by the design team to facilitate iterative blade design modifications to ensure the probability that critical loads will be sustained during system life-cycle are low. An integration of a stochastic-based UQ framework is again re-enforced through this example as it facilitates intelligent data driven decision making.

The uncertainty in CBM$_{max.}$ is presented in Figure 10d. Here the expected BM interval due to input uncertainty is extreme with an expected range of $\approx 31 - 70$ Nm that is $\approx 91\%$ of baseline. In the parametric analysis in Figure 6c, an extended scatter of CBM$_{max.}$ was established due to the variability in SF. This distribution was also shown to be sensitive to small changes in blade stiffness with stiffer and/or softer blades about the baseline (Sf=1.0) resulting in significant deviations in CBM$_{max.}$. This pattern is further re-enforced in the uncertainty analysis (Fig. 10d) with the quantification of extended CBM$_{max.}$ uncertain envelope. In this result, it is also noted that the baseline result at 33.75 Nm is near the lower region of the established 95% probability interval of 30.88 Nm, and to understand this result, the PDF and CDF of the 500,000 Monte Carlo samples is generated in Figure 11.

The PDF of CBM$_{max.}$ in Figure 11a is formed using the maximum likelihood estimation (MLE) method to determine the parameters of a probability distribution that fit the sampled CBM$_{max.}$ data. Based on the fitting analysis, the PDF follows the Generalized Extreme Value (GEV) distribution that is positively skewed with mode (most frequent data represented by the peak of the curve) equalling 35.75 Nm that is close to baseline at 33.75 Nm. The PDF further confirms extreme data outliers are present with high bending moments. Accordingly the extreme value theory (EVT) allows for the interpretation of inferences of extreme deviations where at the tails, CBM$_{max.}$ exceeds 60.00 Nm. As next step, the probabilities of the observations are established using a CDF in Figure 11b. The shaded region represents the symmetric 95% probability interval width (i.e., difference between 2.5% and 97.5% cumulative probability bounds in the dotted green lines), and the probability that: **(a)** Pr. CBM$_{max.} \leq$ 33.75 Nm (baseline) = 10%; or Pr. CBM$_{max.} \geq$ 33.75 Nm (baseline) = 90%; and

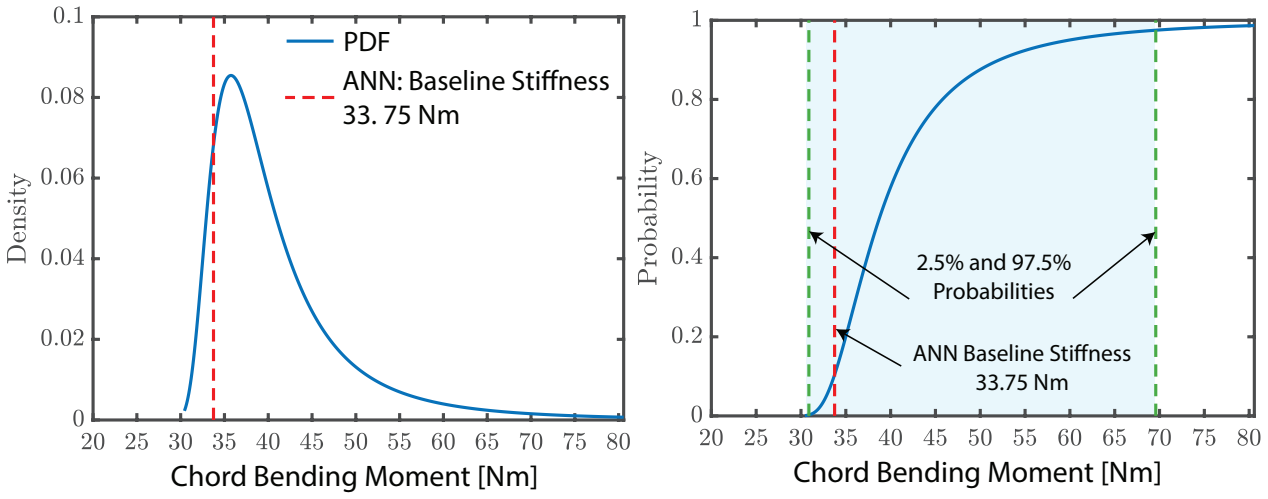

(a) Probability Density Function

(b) Cumulative distribution function

Figure 11: Statistical representation of the uncertainty in CBM$_{max.}$

(b) assuming a safety load factor of 1.50 is applied to the baseline, hence limiting CBM$_{max.}$ = 33.75*1.50 to 50.63 Nm, the probability that CBM$_{max.}$ $\leq$ 50.63 Nm (load factor limit) is $\approx 88\%$.

In the PDF (Fig. 11a) and CDF (Fig. 11b) representation of CBM$_{max.}$, it is noted that the curves are truncated at the extreme ends of the design envelope. This is as a result of constraining the sampling space to realistic SF magnitudes in Figure 12 based on the analysis presented in Figures 7 and 8 to ensure extremely stiff and soft blades that are beyond normal manufacturing tolerances are not considered in the probabilistic analysis. Further, at the extreme tail regions of the design space, the accuracy of the ANN to yield acceptable generalization performance is degraded (Fig. 7), hence the sampling space is constrained to $0.60 \leq$ SF ≤ 1.40 intervals.

4.3. ANN Development: GJ, EI$_{flap}$, EI$_{lag}$ $\rightarrow$ spanwise structural loads

In this section, an ANN is developed and validated to model the relationship between blade stiffness properties and structural loads across 16 r/R span stations. The neural networks formed required two-to-three hidden layers, and in each layer 30 to 40 neurons were needed. To train the network, the Bayesian regularization backpropagation method was used to update the weights and bias values according to Levenberg-Marquardt optimization algorithm. The methodology minimizes a combination of squared errors and weights to then establish a combination of values that form a network with acceptable generalization capabilities.

A total of 1500 RCAS points are generated using LHS from the aleatory distribution of the input parameters in Table 2. RCAS simulations are then simulated using parallel computing per the DAKOTA/GALAXY architecture introduced in Figure 3. The 1500 points are then partitioned into ratios of training, testing, and validation categories. Table 4 demonstrates the accuracy of the network on the testing dataset for a network trained using: a minimum of 150 points; and 1050 representing the maximum training size.

The performance of the ANN in Table 4 is represented by the $r-$correlation measure which assesses the goodness-of-fit between ANN approximation and target RCAS. The results confirm that the ANN demonstrates acceptable generalization capabilities for each of the four outputs. Critically it is also noted that the network trained using 150 data points yielded similar accuracy limits in comparison to a network trained using a larger training sample set of 1050 points. Yet, despite the high accuracy of the ANN, it is noted that the approximation of spanwise TM using a network with 150 points was limited with a lower $r-$correlation measure of 0.924 (shaded in Table 4) than other converged results. Upon further analysis, it was confirmed that data points with poor approximation capabilities that resulted in the lowering of the $r-$correlation metric for span TM was attributed to inputs that were at the tail ends of the normal distribution curve. Recall, an ANN trained with data that is sampled from a PDF, in this case a normal distribution curve, by definition the training sample set will be limited at the tail ends of the PDF curve, and the resulting generalization capabilities of the surrogate-model at these extreme design regions will be limited.

It is also noted that the generalization capabilities of the ANN in approximating rotor power has been reduced in comparison to the data that was presented in Table 3 where the ANN was trained using 490 points. It is important to consider that the data used to assess

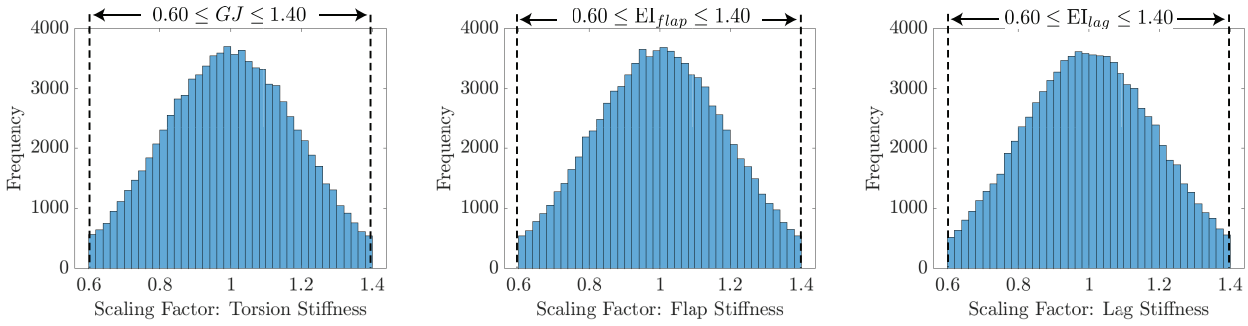

(a) GJ (b) EI_{flap} (c) EI_{lag}

Figure 12: Constraining the uncertain parameter space to realistic stiffness (SF) magnitudes

Table 4: ANN generalization capabilities assessed on the 210 testing points

Uncertain Inputs	Train Size	Test Size	Power	Span TM	Span FBM	Span CBM
			$r-$coefficient			
GJ, $\mathrm{EI}_{\mathrm{flap}}$, $\mathrm{EI}_{\mathrm{lag}}$	150	1350	0.989	0.924	0.997	0.976
	1050	450	0.995	0.989	0.999	0.996

the accuracy of the ANN in Tables 3 (=210 test points) and 4 (=1350 and 450 test points) differ both in sample size and data test points, hence comparisons between the two results cannot be assessed with confidence as it assessed on differing datasets. Despite the noted differences between the two results, the $r-$correlation measure assessed in Table 4 is high at 0.989 and 0.995 for a network trained using 150 and 1050 inputs respectively, hence indicating a strong positive relationship between surrogate-based approximations and RCAS target.

To further demonstrate the accuracy of the ANN, spanwise structural loads is approximated using the two networks from Table 4 at arbitrarily selected stiffness settings. The surrogate-based results are evaluated against RCAS target in Figure 13. In each of the spanwise structural loads results, it is noted that there is excellent agreement between ANN-based predictions using the two networks and RCAS target. The half peak-to-peak loads are captured with precision, and the spanwise structural loads across the 16 radial stations from root-to-tip are resolved with indistinguishable difference between an 150 and 1050 trained network. It is also noted that the ANN tested in Figure 13 reflects SF values that lie between $\mu - 1\sigma$ (FBM with SF=0.80) and $\mu + 2\sigma$ (TM with SF=1.40) intervals which equates to $\approx 81\%$ area under a normal distribution curve or $\approx 81\%$ of representative SF values. The validated performance of the ANN through the visual representation of the spanwise structural loads data, and the high $r-$correlation measure in Table 4 confirms that an ANN trained using only 150 points will yield accurate representation of rotor power and loads due to blade stiffness variability. Accordingly, the surrogate-based approach can be used for uncertainty propagation efforts to follow.

4.4. Uncertainty Analysis: GJ, EI_{flap}, $\mathrm{EI}_{lag} \rightarrow$ spanwise FBM

In this section, the uncertainties in spanwise FBM are quantified using an ANN. The surrogate-based approach utilized is representative of an ANN that is trained using 1050 training points from Table 4. The effect of Monte Carlo sample size, n, on statistical convergence for the generation of the 95% probability intervals is presented in Figure 14.

In Figure 14a, it is noted that the scope of the 95% probability intervals generated using $n = 1000$ Monte Carlo points does not generate accurate intervals across the blade span, compared to large datasets. The results formed using $n = 10,000$ and $n = 500,000$ are in agreement, yet the results quantified using $n = 1000$ points illustrate non-convergence at the 2.5% probability side, most notably at span stations 8-10 and at station 14, yet at the 97.5% probability side the agreement is acceptable. To confirm data non-convergence at $n = 1000$ compared to $n = 500,000$, the PDF at span station 8 is presented in Figure 14b. It is confirmed that the data generated using $n = 1000$ points results in a PDF with less overall area under the curve, hence limiting the FBM intervals at the 2.5% and 97.5% level. Alternately, the PDF formed using $n = 500,000$ points is characterized with a larger area under the PDF curve as the design space has been adequately mapped, and the updated

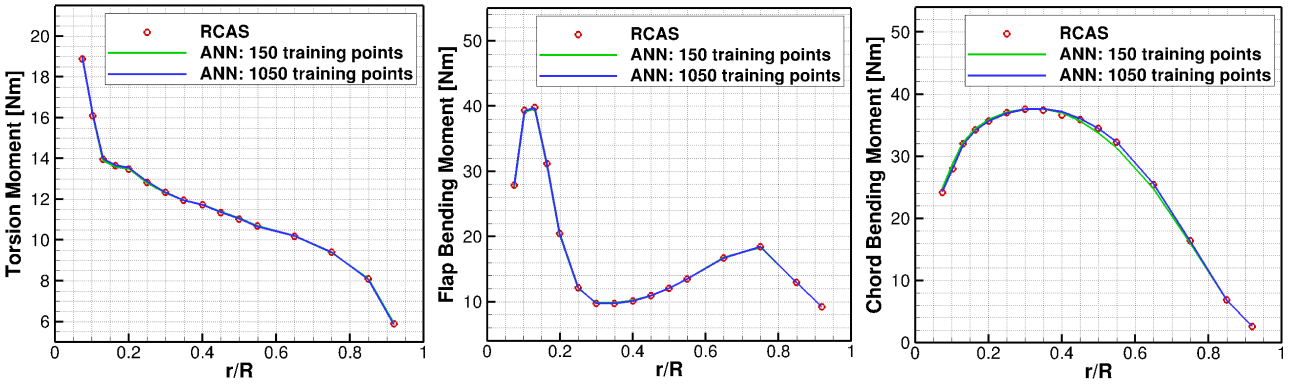

(a) Distribution of TM at SF=1.40 (b) Distribution of FBM at SF=0.80 (c) Distribution of CBM at SF=1.20

Figure 13: Evaluation of spanwise bending moment prediction using ANN with RCAS

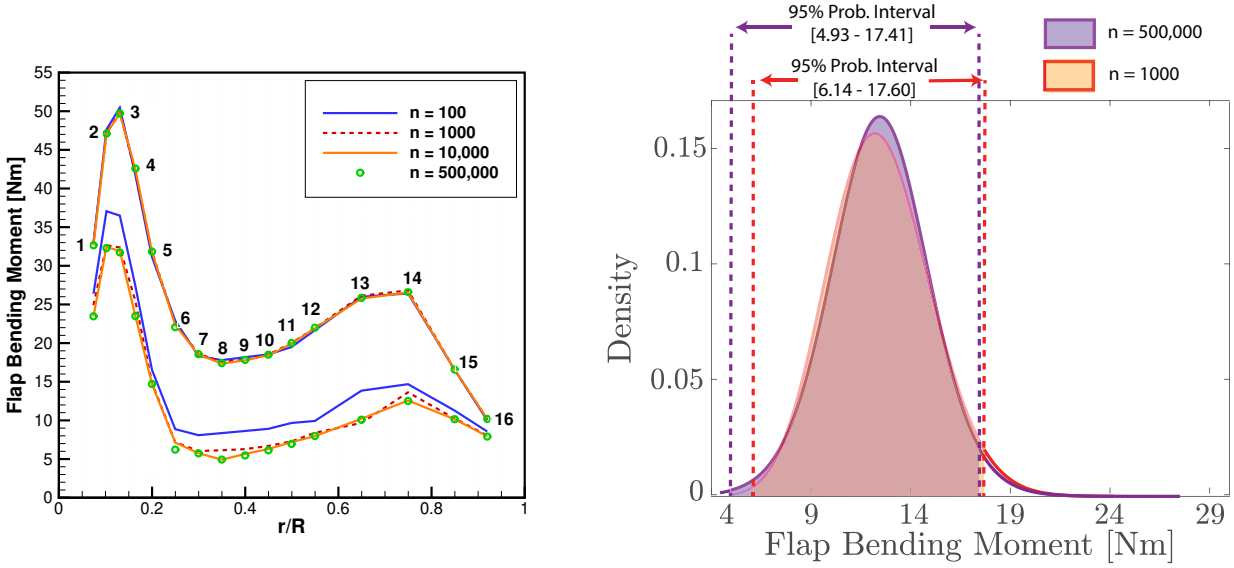

(a) 95% probability intervals

(b) PDF at station 8 - $r/R = 0.35$

Figure 14: Convergence of FBM uncertainty analysis using Monte Carlo simulations as a function of sample size, n

probability intervals reflect this new and extended design space. Further, the computational overheads required to simulate data using an ANN is negligible, hence large datasets can be processed. Hence, in this analysis a Monte Carlo simulation with 500,000 LHS generated points are used to form the 95% probability intervals in Figure 15.

In Figure 15, the spanwise FBM at the baseline stiffness (SF=1.0) is established using RCAS with an 8×8 dynamic inflow model which is in agreement with ANN estimation across each blade span station. The computational data (RCAS and ANN) are also in agreement with available experimental data ($\circ$) at radial stations 7,9,12,13 and 14. At radial station 15, there is a disagreement between the datasets which is attributed to the RCAS inflow state model. Figure 16 validates that an 8×8 inflow model used in this analysis is not sufficient to accurately resolve FBM at radial station 15 while a 12×12 model yields improved agreement.

Even though the accuracy of the ANN to resolve spanwise structural loads was validated in Table 4 and Figure 13, additional validation analysis is presented to justify the difference between computational and experimental data at r/R station 15, and the proximity of the experimental data converging to the lower band of the 95% probability interval (Fig. 15). The noted differences are attributed to the setup of the dynamic inflow model (Fig. 16) and is not a limitation of the surrogate model. To confirm this assessment, the accuracy of the ANN trained using 1050 inputs and evaluated using 450 test points (Table 4) is demonstrated using the $r-$correlation goodness-of-fit measure for FBM at r/R stations 1,5,8 and 15 in Figure 17

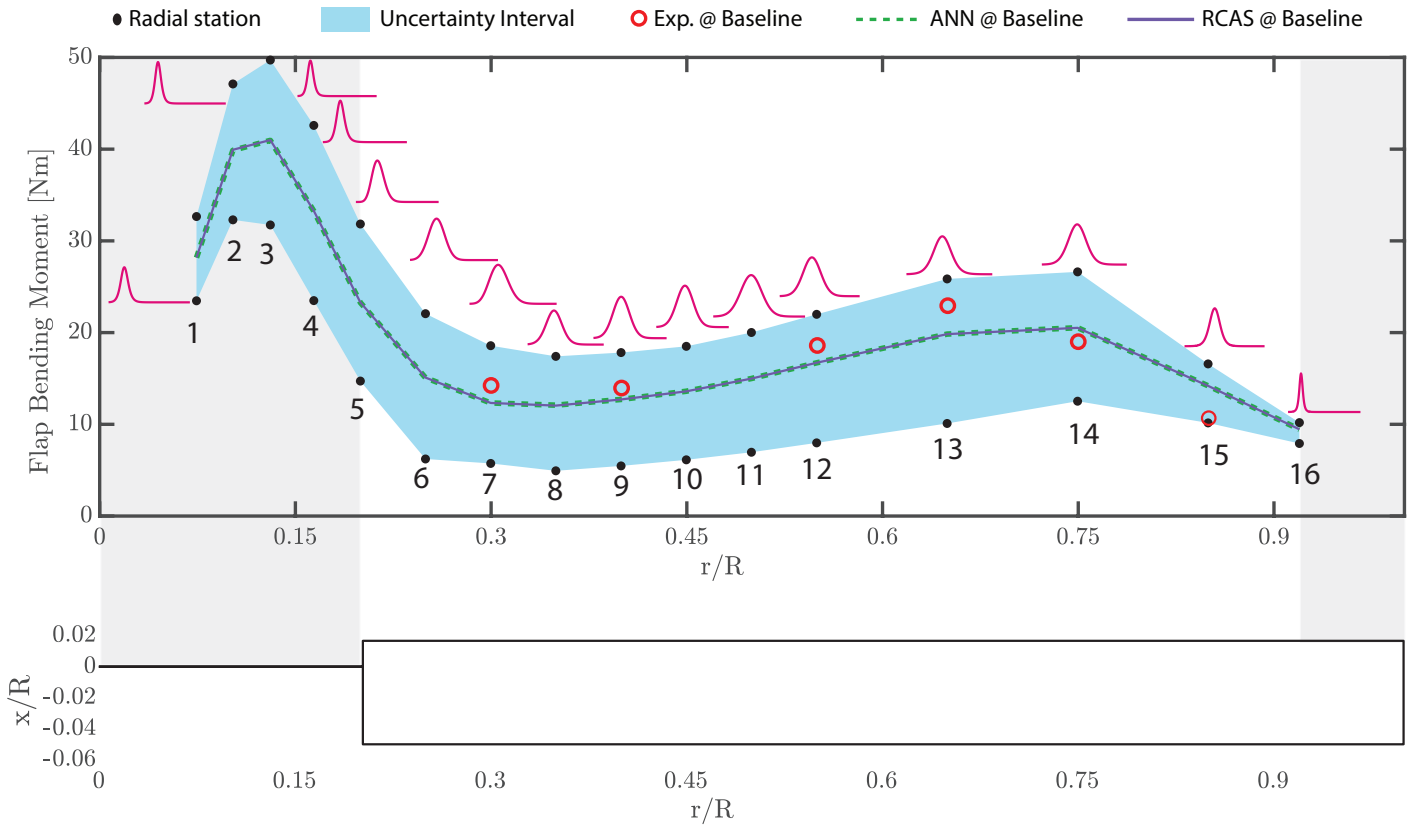

Figure 15: Uncertainty distribution of spanwise FBM using 500,000 Monte-Carlo sample points

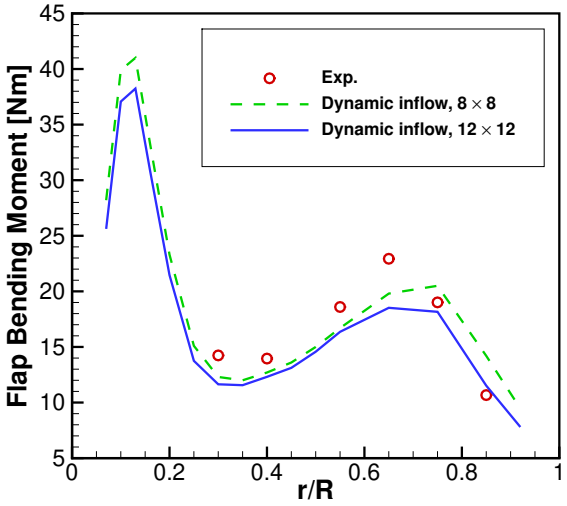

Figure 16: Half peak-to-peak FBM convergence using an 8×8 and 12×12 dynamic inflow modelwith test data

The $r-$correlation charts confirm that a perfect agreement between RCAS target and ANN estimations is present at the outlined r/R span stations. The validation test confirms that the disparity of the experimental point at radial station 15 to the computational data, and the proximity toward the lower end of the 95% probability interval is attributed to the selection of an 8×8 dynamic inflow model. Instead if uncertainty propagation was executed using a 12×12 dynamic inflow model, the disparity between the stated datasets would be negligible.

The distribution of the uncertainty intervals is now analyzed. The blue shaded region in Figure 15 represents the 95% probability interval established from the CDF of the 500,000 LHS generated points. The greyed region represents areas of the blade that have high stiffness due to the placement of the flap/lag hinges and pitch bearing about the inboard blade sec-

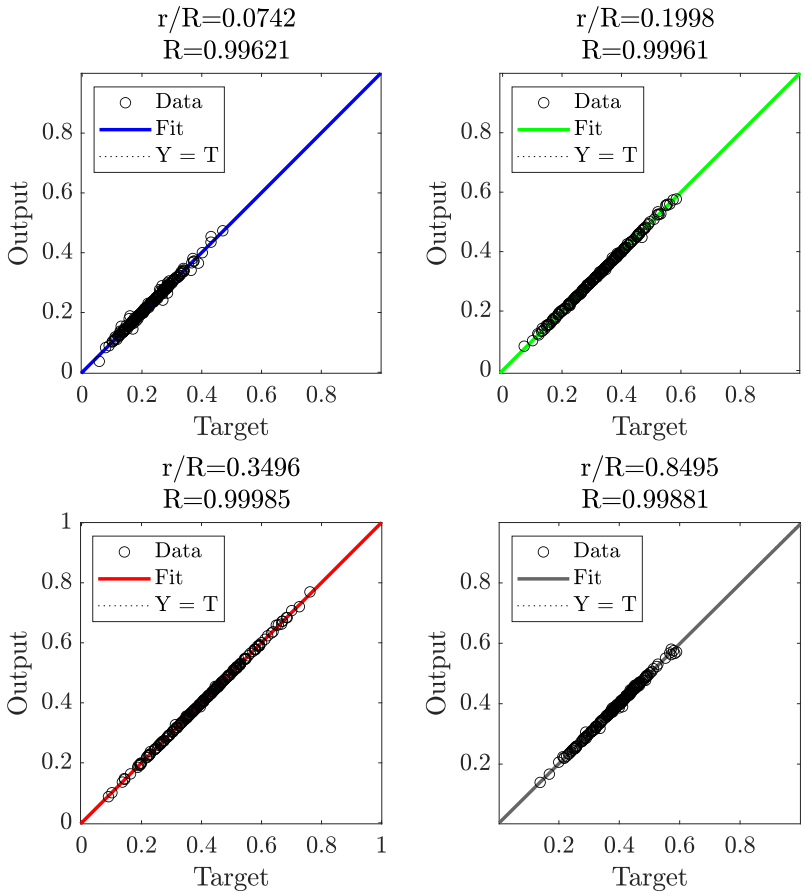

Figure 17: ANN validation of FBM at prescribed r/R spanwise stations against RCAS target using the $r-$coefficient metric

tions (Fig. 1). The FBM is expected to be zero at blade inboard hinge location and the tip due to the enforcement of zero moment boundary condition in RCAS, hence the datasets comprising RCAS, ANN and probability interval width decrease and converge at these regions. Accompanying the probability intervals are the distribution of the converged PDFs that represent the dispersion and degree-of-skewness of FBM at the respective r/R stations. The PDFs at radial stations 1-5 are characterized with high *skewness* and *kurtosis*; both metrics that involve the assessment of the data in the tails of the distribution. The skewness assesses the symmetry of the distribution, and a symmetric distribution is modeled such that the right and left sides of the PDF follow a similar shape. In this analysis, the skewness of the PDFs at radial stations 1-5 is greater than 0, hence is classified as a right-skewed distribution where the right tail is longer than the left. Equating this observation to FBM translates to a distribution of data where higher sample of FBM (data *mode* represented by the peak of the PDF curve) are present that have low magnitudes than high which are present in the extreme tails. Conceptually this is justifiable as the blade at these regions is very stiff. A positively skewed PDF conveys the direction of data outliers, and in this case, the outliers are present on the right side of the distribution where FBM magnitudes are high. Kurtosis is also factored in the analysis and assesses the amount of probability in the tails. The metric is defined as *"a measure of the combined weight of the tails relative to the rest of the distribution"* [36]. The kurtosis magnitude is evaluated against the kurtosis of a normal distribution, which is equal to 3. If the kurtosis is greater than 3, then the dataset has heavier tails than a normal distribution (more data in the tails), and if the kurtosis is less than 3, then the dataset has lighter tails than a normal distribution (less data in the tails). In Figure 15, the data in the tails at radial stations 1-5 is heavy such that the kurtosis is greater than 3 and is a maximum at station 2 where it is ≈ 19. Translating this pattern to FBM confirms that here are high probabilities of extremely large FBM magnitudes, yet these are limited to outliers in the distribution.

The statistical representation of the PDF distributions from stations 6-15 is relatively symmetrical with medium-tailed data. The *skewness* of the PDFs is $\approx$

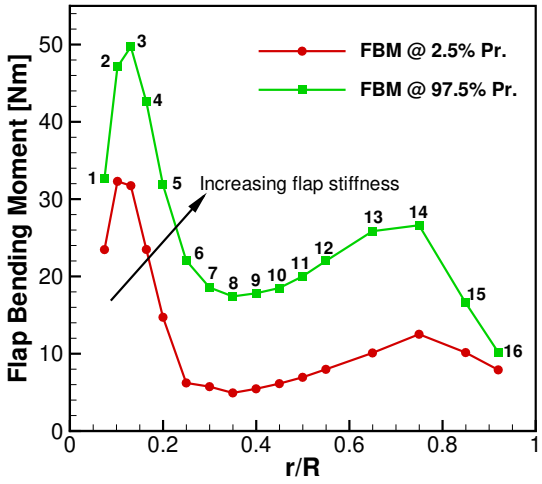

(a) FBM distribution

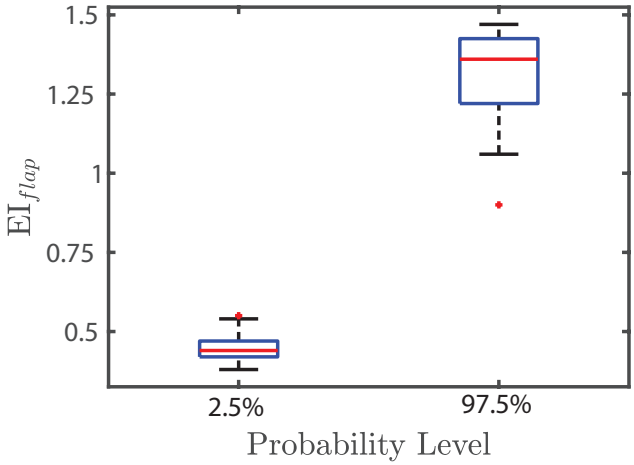

(b) Boxplot representation of the distribution of EI$_{flap}$

Figure 18: Distribution in FBM and EI$_{flap}$ at corresponding probability levels

0, hence representing symmetric distribution of FBM about the center point of the curve. The *kurtosis* in this dataset is ≈ 3, hence confirming medium-tails and data peaks that match the normal distribution. Translating these patterns to FBM equates to data distribution about a central point where FBM outliers are neither highly frequent or highly infrequent. The stiffness of the blade mid-span stations is impacted by the stiffness scaling factor, and the PDF distribution confirms that the expected variability in FBM outcomes is symmetric about a central point with the absence of extreme outliers.

Similarly, the PDF about blade tip region is also analyzed at station 16. Here it is observed that the 95% probability interval is narrow and the data points (RCAS and ANN) are converging to a common point. This is as a result of enforcing a zero moment boundary condition at the tip that results in the lowering of the FBM. Statistically the PDF at this station is positively-skewed with an extended tail representing the distribution of extreme data outliers. The kurtosis is also positively-extreme confirming frequent outliers that have high probability with extreme FBM magnitudes. The extreme positive kurtosis indicates a distribution where there are greater number of FBM data points located in the tails of the distribution instead of around the mean. This pattern matches the data established in stations 1 to 5: blade regions that are naturally stiff will be represented with stochastic data that is skewed about a central point with outliers that are characterized with extreme FBM magnitudes at high probabilities.

As next step, the blade stiffness at the 2.5% and 97.5% probability levels which are used to establish the central 95% probability intervals (shaded area in blue in Fig. 15) are quantified in Table 5. The FBM is further projected at the extreme probability levels for each span station, r/R, in Figure 18a and the distribution of EI$_{flap}$ for the respective probability threshold database is generated using a boxplot in Figure 18b. Figure 18b shows that the FBM at the 2.5% probability interval in Figure 18a is representative of low flap stiffness, as was also quantified in Table 5 (shaded data), and comparatively the higher FBM at the 97.5% probability threshold is denoted with higher flap stiffness at the respective radial stations. The results generated in the probabilistic analysis match the trends in the parametric analysis in Figure 6b where an increase in flap stiffness was accompanied with an increase in FBM. The benefit of a stochastic based approach presented in this analysis facilitates the quantification of observation probabilities which otherwise would not be available with a simplified parametric based approach.

The data in Table 5 also confirms that GJ is higher on the 2.5% probability level (with low FBM) than at the 97.5% threshold (higher FBM) for each corresponding radial station. It is also established that the lag stiffness is comparable at the two probability levels. Figure 19 represents a parametric analysis of the variation in GJ and EI$_{lag}$ on FBM. It is shown that the trends formed in the parametric analysis are consistent with the stochastic data in Table 5 such that: **(a)** as GJ is reduced $\rightarrow$ FBM increases and confirmed in Figure 19a; and **(b)** variability in EI$_{lag}$ has a negligible impact on FBM and confirmed in Figure 19b.

Further it is important to note that the stiffness parameters in Table 5 are not representative of a range of values that would be expected between the established upper and lower limits for FBM$_{min.}$ and FBM$_{max.}$ respectively. Instead they represent the stiffness magnitude for a single blade at the extreme probability threshold. Due to the coupling effects between

Table 5: Blade stiffness at 95% probability interval thresholds for FBM (Fig. 15) using 500,000 Monte-Carlo samples

	2.5% Probability				97.5% Probability			
Span station @ r/R	FBM [Nm]	GJ	EI_{flap}	EI_{lag}	FBM [Nm]	GJ	EI_{flap}	EI_{lag}
1 @ 0.0742	23.47	1.48	0.44	1.28	32.65	0.80	1.24	0.77
2 @ 0.1021	32.30	1.13	0.55	0.66	47.11	0.82	1.36	0.69
3 @ 0.1308	31.74	1.23	0.42	0.73	49.71	0.80	1.40	0.94
4 @ 0.1641	23.49	1.32	0.42	0.95	42.59	0.53	1.06	0.83
5 @ 0.1998	14.72	1.31	0.54	1.44	31.84	0.73	1.40	1.23
6 @ 0.2497	6.22	1.49	0.40	1.03	22.06	0.43	0.90	0.81
7 @ 0.2997	5.74	1.21	0.51	1.05	18.57	0.71	1.36	1.03
8 @ 0.3496	4.93	0.98	0.39	1.11	17.41	1.02	1.47	1.00
9 @ 0.3996	5.46	1.20	0.44	0.86	17.82	0.95	1.46	0.96
10 @ 0.4496	6.13	1.12	0.44	1.15	18.50	1.01	1.46	1.13
11 @ 0.4995	6.95	1.05	0.44	0.68	20.01	0.59	1.19	0.71
12 @ 0.5495	7.98	1.13	0.46	0.76	22.00	1.06	1.45	0.84
13 @ 0.6495	10.10	0.92	0.43	0.84	25.85	0.60	1.24	0.71
14 @ 0.7495	12.52	1.06	0.46	1.00	26.62	0.76	1.32	0.72
15 @ 0.8495	10.15	1.00	0.48	0.80	16.59	0.76	1.40	1.15
16 @ 0.9195	7.91	1.08	0.38	1.04	10.19	0.63	1.20	1.07

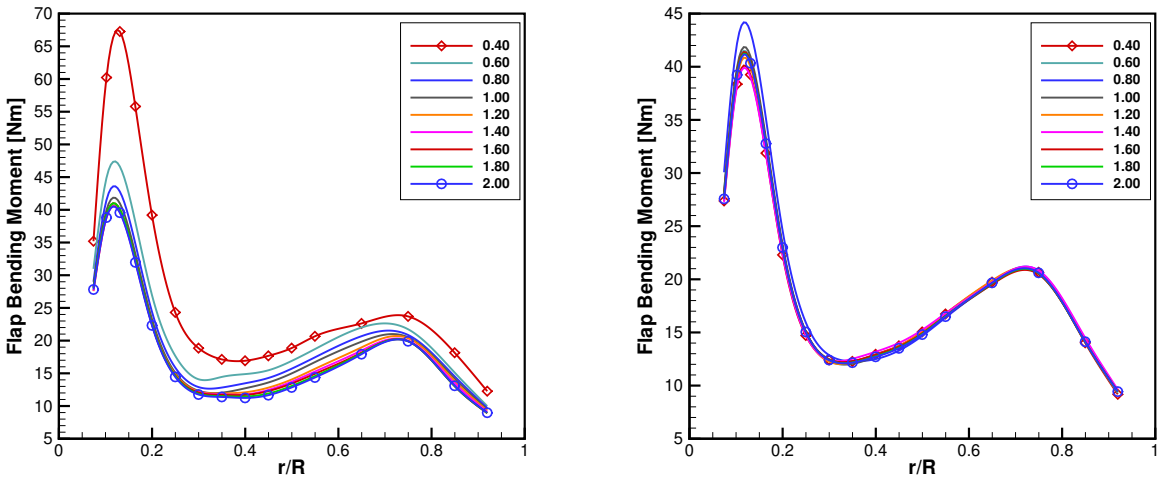

(a) GJ on FBM

(b) EI_{lag} on FBM

Figure 19: Parametric analysis representing the relationship between GJ and EI_{lag} on FBM

the three stiffness parameters, there may exist blades with lower and higher stiffness magnitudes than the data reported in Table 5 even if the equating FBM is within the established intervals. In future works, additional data analysis will be warranted to qualitatively represent the distribution of stiffness magnitudes in the established FBM probability design space to aid informed decision making in the event stiffness settings exceed allowable design thresholds.

5. Conclusion

An uncertainty quantification framework for rotorcraft aeromechanics was introduced. The analysis focused on characterizing and modeling the effect of aleatory uncertainties that are normally distributed in the ONERA 7A blade including torsion, flap, and lag stiffness on rotor performance and loads at high speed. A surrogate-based approach using artificial neural networks was introduced to support large-scale data analysis required to establish the uncertainty intervals using statistical metrics. Two case studies with

response outputs-of-interest were considered in the analysis: **(1)** rotor power and half peak-to-peak torsion, flap, and chord bending moment amplitudes; and **(2)** spanwise structural loads from blade root to tip. Uncertainty quantification was executed using a Monte Carlo approach with LHS, and the analysis confirmed that uncertainties in rotor power are relatively negligible, yet significant uncertainties were quantified for the estimation of peak FBM, and most significant uncertainties were attributed to the estimation of peak CBM. The work then progressed to the quantification of uncertainties in spanwise flap bending moment across 16 radial stations. The analysis showed that uncertainty intervals are reduced at the blade inboard and tip regions due to zero moment boundary conditions at the flap hinge and blade tip. At other regions, the uncertainty intervals are consistent in magnitude relative to the nominal condition when no uncertainties are factored. For the assumed uncertainty distribution, this analysis shows that both flap and torsion stiffness influence the uncertainty in spanwise flap bending moment, yet lag stiffness has a negligible impact.

6. Future Work

As next steps, the analysis will be extended to model the spanwise uncertainty due to stiffness on torsion and chord bending moment. A global sensitivity analysis will also be undertaken to identify blade regions where uncertainties are most sensitive to input stiffness. The analysis will also be undertaken at high-thrust setting to establish if the uncertainty patterns established in this analysis are also consistent at other flight conditions. Finally, an accurate representation of the basis of the input uncertainty distribution needs to be quantified so that a realistic representation of output uncertainties can be formed.

References

[1] Andrew M. Wissink, William J. Staruk, Steven A. Tran, Beatrice Roget, Vinod K. Lakshminarayan, Jayanarayanan Sitaraman, and Buvaneswari Jayaraman. Overview of New Capabilities in Helios Version 9.0. In *57th AIAA Scitech Forum*, San Diego, CA, January 7–11 2019.

[2] H. Saberi, M. Hasbun, J. Y. Hong, H. Yeo, and R. A Ormiston. Overview of RCAS Capabilities, Validations, and Rotorcraft Applications. In *American Helicopter Society 71st Annual Forum*, Virginia Beach, VA, May 5–7 2015.

[3] Dinesh Kumar, Yao Koutsawa, Gaston Rauchs, Mariapia Marchi, Carlos Kavka, and Salim Belouettar. Efficient Uncertainty Quantification and Management in the Early Stage Design of Composite Applications. *Composite Structures*, 251:112538, 2020.

[4] Itham Salah El Din, Manas Khurana, and Hyeonsoo Yeo. Towards Uncertainty Quantification of the ONERA 7A Rotor using Comprehensive Analysis. In *47th European Rotorcraft Forum*, Virtuel, France, September 2021.

[5] B. Ortun, M. Potsdam, H. Yeo, and K. Truong. Rotor Loads Prediction on the ONERA 7A Rotor Using Loose Fluid/Structure Coupling. *Journal of the American Helicopter Society*, 62(3):032005–1–032005–13, 2017.

[6] P. Beaumier, M. Costes, B. Rodrigues, M. Polnot, and B Cantaloube. Weak and Strong Coupling Between the elsa CFD Solver and the HOST Helicopter Comprehensive Analysis. In *31st European Rotorcraft Forum*, Florence, Italy, September 13–15 2005.

[7] Hyeonsoo Yeo, Mark Potsdam, Biel Ortun, and Khiem Van Truong. High-Fidelity Structural Loads Analysis of the ONERA 7a Rotor. *Journal of Aircraft*, 54(5):1825–1839, 2017.

[8] Klausdieter Pahlke and Berend G. van der Wall. Chimera Simulations of Multibladed Rotors in High-Speed Forward Flight with Weak Fluid-Structure-Coupling. *Aerospace Science and Technology*, 9(5):379–389, 2005. Rotorcraft Research.

[9] Costes M. Beaumier, P. and R. Gavériaux. Comparison Between FP3D Full Potential Calculations and S1 Modane Wind Tunnel Test Results on Advanced Fully Instrumented Rotors. In *19th European Rotorcraft Forum*, Como, Italy, September 14-16, 1993.

[10] M. D. McKay, R. J. Beckman, and W. J. Conover. Comparison of Three Methods for Selecting Values of Input Variables in the Analysis of Output from a Computer Code. *Technometrics*, 21(2):239–245, 1979.

[11] Andrea Gamannossi, Alberto Amerini, Matteo Poggiali, Carlo Alberto Elmi, Lorenzo Mazzei, and Antonio Andreini. Uncertainty quantification of an aeronautical combustor using a 1-D approach. *AIP Conference Proceedings*, 2191(1):020083, 2019.

[12] John Schaefer, Serhat Hosder, Thomas West, Christopher Rumsey, Jan-Renee Carlson, and William Kleb. Uncertainty quantification of turbulence model closure coefficients for transonic wall-bounded flows. *AIAA Journal*, 55(1):195–213, 2017.

[13] Dunn M.C, Babak Shotorban, and Abdelkader Frendi. Uncertainty Quantification of Turbulence Model Coefficients via Latin Hypercude Sampling method. *Journal of Fluids Engineering*, 133, 04 2011.

[14] H. García-Alfonso and D. Córdova-Esparza. Comparison of Uncertainty Analysis of the Montecarlo and Latin Hypercube Algorithms in a Camera Calibration Model. In *2018 IEEE 2nd Colombian Conference on Robotics and Automation (CCRA)*, pages 1–5, Nov 2018.

[15] Review of Improved Monte Carlo Methods in Uncertainty-Based Design Optimization for Aerospace Vehicles. *Progress in Aerospace Sciences*, 86:20 – 27, 2016.

[16] Robert Scott and Manas S. Khurana. Conceptual Design and Assessment of a Light Multirole Rotorcraft Using Uncertainty Quantification. In *AIAA Scitech 2019 Forum*, San Diego, CA, 7-11 January 2019.

[17] Manas S. Khurana, Carl R. Russell, and Robert Scott. Uncertainty Quantification of a Rotorcraft Conceptual Sizing Toolsuite. In *AIAA Scitech 2019 Forum*, San Diego, CA, 7-11 January 2019.

[18] Dirk Gorissen, Karel Crombecq, Ivo Couckuyt, and Tom Dhaene. *Automatic Approximation of Expensive Functions with Active Learning*, pages 35–62. Springer Berlin Heidelberg, Berlin, Heidelberg, 2009.

[19] Lak V Lakshmanan, Michael Munn, and Sara Robinson. *Machine Learning Design Patterns*. 2020.

[20] Wanggang Shen, Xun Huan, Beckett Yx Zhou, and Nicolas R. Gauger. Towards Design of Airfoil Pressure Tap Locations for Real-Time Predictions Under Uncertainty Using Bayesian Neural Networks. In *AIAA Scitech 2020 Forum*, Orlando, FL, 2020.

[21] Sicheng (Kevin) Li and Seongkyu Lee. A Machine Learning-Based Fast Prediction of Rotorcraft Broadband Noise. In *AIAA Aviation 2020 Forum*, Virtual Event, 2020.

[22] Chintan Patel and Chad Iverson. Parametric Design Optimization in Computational Aerodynamics using Artificial Deep Neural Networks. In *AIAA Propulsion and Energy 2020 Forum*, Virtual Event, 2020.

[23] Seong Hyeon Hong, Yi Wang, and Yang Yu. Model Predictive Control of Quadcopter Using Physics-Guided Neural Network. In *AIAA SCITECH 2022 Forum*, San Diego, CA, 2022.

[24] Wayne Farrell and Michael Kinzel. Modeling UAVs using CFD and Machine Learning Methods. In *AIAA SCITECH 2022 Forum*, San Diego, CA, 2022.

[25] Yvan Tondji, Georges Ghazi, and Ruxandra M. Botez. CRJ 700 Aerodynamic Coefficients Identification in Dynamic Stall Conditions using Neural Networks. In *AIAA SCITECH 2022 Forum*, San Diego, CA, 2022.

[26] Vinothkumar Sekar, Mengqi Zhang, Chang Shu, and Boo Cheong Khoo. Inverse Design of Airfoil Using a Deep Convolutional Neural Network. *AIAA Journal*, 57(3):993–1003, 2019.

[27] Ben D. Phillips and Christopher Heath. System-Level Impact of Propulsive Uncertainties for Low-Boom Aircraft Concepts. In *AIAA Aviation 2020 Forum*, Virtual Event, 2020.

[28] Yutian Pang, Yuhao Wang, and Yongming Liu. Probabilistic Aircraft Trajectory Prediction with Weather Uncertainties using Approximate Bayesian Variational Inference to Neural Networks. In *AIAA Aviation 2020 Forum*, Virtual Event, 2020.

[29] Jie Chen and Yongming Liu. Physics-Guided Machine Learning for Multi-Factor Fatigue Analysis and Uncertainty Quantification. In *AIAA Scitech 2021 Forum*, Virtual Event, 2021.

[30] Jianhua Yin and Xiaoping Du. Uncertainty Quantification by Convolutional Neural Network Gaussian Process Regression with Image and Numerical Data. In *AIAA SCITECH 2022 Forum*, San Diego, CA, 2022.

[31] Nathan Harl, Karthikeyan Rajagopal, and S. N. Balakrishnan. Neural Network Based Modified State Observer for Orbit Uncertainty Estimation. *Journal of Guidance, Control, and Dynamics*, 36(4):1194–1209, 2013.

[32] The MathWorks. *Deep Learning Toolbox*. The MathWorks, Inc., Natick, Massachusetts, United States, 2022.

[33] B.M. Adams, L.E. Bauman, W.J. Bohnhoff, K.R. Dalbey, M.S. Ebeida, J.P. Eddy, M.S. Eldred, P.D. Hough, K.T. Hu, J.D. Jakeman, J.A. Stephens, L.P. Swiler, D.M. Vigil, and T.M. Wildey. Dakota, A Multilevel Parallel Object-Oriented Framework for Design Optimization, Parameter Estimation, Uncertainty Quantification, and Sensitivity Analysis: Version 6.0 User's Manual. Technical report, Sandia Technical Report SAND2014-4633, July 2015.

[34] Galaxy: A Framework for Multi-Site, Cross-Platform Simulation and Optimization. White Paper. Technical report, Directed Energy Directorate of the Air Force Research Lab and Stellar Science Ltd Co, July 2018.

[35] R. Jain and H. Yeo. Effects of Torsion Frequencies on Rotor Performance and Structural Loads with Trailing Edge Flap. *Smart Material Structures*, 21(8):085026, August 2012.

[36] Donald J. Wheeler. Problems with Skewness and Kurtosis, Part One - What do the Shape Parameters do? *Quality Digest Daily*, (231), August, 2011.